Rossby wave instability and apparent phase speeds in large ocean basins

P.E. Isachsen[1], J. H. LaCasce[1,2,3] and J. Pedlosky[3]

1- Dept. of Geosciences, University of Oslo, Oslo, Norway
2- Norwegian Meteorological Institute, Oslo, Norway
3- Woods Hole Oceanographic Inst., Woods Hole, MA

Submitted to J. Phys. Oceanogr.
17th November 2005

Corresponding author address:
Joe LaCasce
Norwegian Meteorological Institute
P.O. Box 43 Blindern
0313 Oslo, Norway
jlacasce@met.no

Abstract

We examine the stability of baroclinic Rossby waves in large ocean basins, generalizing the quasi-geostrophic results of LaCasce and Pedlosky (2004). We derive stability equations applicable for large scale waves using the two layer shallow water system. Under these equations, unstable perturbations at a given latitude are nearly geostrophic. The equations resemble the quasi-geostrophic stability equations except that they retain the full variation of the deformation radius with latitude. We solve these equations numerically for different initial conditions, by calculating eigenmodes and time-stepping. The fastest growing eigenmodes are intensified at high latitudes and slower modes at lower latitudes; all the modes have meridional scales comparable to the local deformation radius and growth rates inversely proportional to the deformation radius. These points are all consistent with the quasi-geostrophic results.

We then simulated the evolution of large scale waves using the ROMS primitive equation model. The results are consistent with the theoretical predictions, with deformation-scale perturbations growing at rates inversely proportional to the deformation radius. The waves succumb to the perturbations at the mid- and high latitudes, but are able to cross the basin at low latitudes before doing so. And the barotropic waves produced by the instability propagate faster than the baroclinic long wave speed, which may explain the discrepancy in speeds noted by Chelton and Schlax (1996).

1 Introduction

Quasi-geostrophic studies suggest that baroclinic Rossby waves are unstable (Jones, 1979; Vanneste, 1995; LaCasce and Pedlosky, 2004, LP04 hereafter). The waves break into deformation-scale eddies, on a time scale proportional to the ratio of the deformation radius to the shear velocity, i.e. $T_g \propto L_D/U$. Instability occurs because waves that are generated at the eastern oceanic boundary tend to have their crests oriented meridionally and thus cannot be stabilized by the β-effect (Pedlosky, 1987). Since the instability occurs essentially for *all* oceanic Rossby waves regardless of amplitude or latitude, the only question is how long before the wave succumbs to instability. In other words, if a Rossby wave emanates from the eastern boundary of the basin, can it cross to the western boundary before disintegrating?

The answer depends on the ratio of the crossing time to the unstable growth time, defined as Z by LP04. Since the crossing time for a long baroclinic wave is $L_B(\beta L_D^2)^{-1}$ (where L_B is the basin width), we have:

$$Z \equiv \frac{T_R}{T_g} = \frac{UL_B}{\beta L_D^3}\ . \tag{1}$$

Waves can cross intact if Z is less than order one.

The theory of LP04 makes three specific predictions vis a vis the oceanic Rossby wave field. First, large scale baroclinic waves should be seen only at low latitudes, where Z is small. Because Z varies so strongly with the deformation radius, the latitudinal transition between crossing and disintegrating waves should be sharp. Using representative values for the Pacific, LP04 suggested this critical latitude is about 20 degrees. This is roughly consistent with satellite observations of sea surface height, where large scale propagation is only visible at latitudes lower than about 20 degrees (Chelton and Schlax, 1996).

Second, the dominant eddy scale north of the critical latitude (in the northern hemisphere) should be larger than the deformation radius. This is because the most unstable mode has a meridional scale of roughly twice the deformation radius. Such a shift in

scale is also consistent with satellite observations (Stammer, 1997). If, in addition, the barotropic eddies produced by instability merge, they will produce still larger barotropic waves. This can be seen in numerical experiments when $Z > 1$ (LP04).

Third, the westward phase propagation observed at the mid- and high latitudes should occur at speeds faster than the baroclinic long wave speed. This is because the most unstable barotropic waves propagate faster than long baroclinic waves. This too is consistent with satellite observations (Chelton and Schlax, 1996). If eddy merger occurs, yielding larger barotropic waves, still higher speeds will occur.

Thus in these respects the theory is in agreement with observations. However, it is not strictly correct to apply quasi-geostrophic (QG) theory to large basins. QG assumes the deformation radius is constant and this is certainly not the case; in the Pacific, the deformation radius varies from several hundred kilometers at low latitudes to a few kilometers at high latitudes. LP04 suggested the QG results should apply locally, over a latitude band, and could thus be used to infer in a piecewise fashion the behavior of the large scale wave. But this remained to be demonstrated.

Hereafter we consider the stability of baroclinic Rossby waves in large basins, like the Pacific. We first develop a theory in which the basic baroclinic wave evolves under the shallow water equations, but the unstable perturbations are locally quasi-geostrophic. We examine solutions of this system numerically. Then we use the ROMS primitive equation model to study the evolution of similar large baroclinic waves. The results of the computations are consistent with the theory, and moreover support the predictions from QG theory.

2 The LQG Model

2.1 Equations

We assume a two layer ocean under the shallow water approximation (e.g. Pedlosky, 1987):

$$\frac{\partial}{\partial t}\vec{u}_1 + \vec{u}_1 \cdot \nabla \vec{u}_1 + f\hat{k} \times \vec{u}_1 = -g\nabla\chi \tag{2}$$

$$\frac{\partial}{\partial t}\vec{u}_2 + \vec{u}_2 \cdot \nabla \vec{u}_2 + f\hat{k} \times \vec{u}_2 = -g\nabla\chi - g'\nabla\eta \ , \tag{3}$$

where $\vec{u}_1$ and $\vec{u}_2$ are the layer velocities, χ the sea surface height and η the interface height. We have taken the layers to have equal depth, H/2 (an unrealistic assumption but one which simplifies the derivation and does not alter the results qualitatively). From these layer equations, we derive equations for the barotropic and baroclinic velocities:

$$\frac{\partial}{\partial t}\vec{u}_B + \vec{u}_B \cdot \nabla \vec{u}_B + \frac{1}{4}\vec{u}_T \cdot \nabla \vec{u}_T + f\hat{k} \times \vec{u}_B = -g\nabla\chi - \frac{1}{2}\, g'\nabla\eta \equiv -\nabla\phi_B \tag{4}$$

$$\frac{\partial}{\partial t}\vec{u}_T + \vec{u}_T \cdot \nabla \vec{u}_B + \vec{u}_B \cdot \nabla \vec{u}_T + f\hat{k} \times \vec{u}_T = -g'\nabla\eta \equiv -\nabla\phi_T \tag{5}$$

where

$$\vec{u}_B \equiv \frac{1}{2}(\vec{u}_1 + \vec{u}_2), \quad \vec{u}_T \equiv (\vec{u}_2 - \vec{u}_1) \tag{6}$$

are the barotropic and baroclinic velocities. We have defined equivalent barotropic and baroclinic displacements:

$$\phi_B = g\chi + \frac{1}{2}g'\eta, \quad \phi_T = g'\eta \ . \tag{7}$$

to decouple the barotropic and baroclinic equations.

The layer continuity equations are:

$$\frac{\partial}{\partial t}(H/2 + \chi - \eta) + \nabla \cdot (\vec{u}_1(H/2 + \chi - \eta)) = 0 \tag{8}$$

$$\frac{\partial}{\partial t}(H/2 + \eta) + \nabla \cdot (\vec{u}_2(H/2 + \eta)) = 0 \ . \tag{9}$$

We can rewrite these in terms of the barotropic/baroclinic velocities and displacements as follows:

$$\frac{\partial}{\partial t}\phi_T + \frac{g'H}{2}\nabla\cdot(\vec{u}_B + \frac{1}{2}\vec{u}_T) + \nabla\cdot((\vec{u}_B + \frac{1}{2}\vec{u}_T)\phi_T) = 0 \tag{10}$$

$$\frac{g'}{g}\frac{\partial}{\partial t}\phi_B + (\frac{g'}{4g}+1)\,g'H\,\nabla\cdot\vec{u}_B + \frac{g'}{8g}\,g'H\nabla\cdot\vec{u}_T + (\frac{g'}{4g}+1)\nabla\cdot(\vec{u}_T\phi_T) +$$

$$\frac{g'}{g}\nabla\cdot((\vec{u}_B - \frac{1}{2}\vec{u}_T)\phi_B) = 0\,. \tag{11}$$

We will non-dimensionalize the equations, to facilitate the subsequent perturbation expansions. We assume a velocity scale, U, a length scale, L and an advective time scale, $T = L/U$, The resulting equations are then:

$$\epsilon\frac{\partial}{\partial t}\vec{u}_B + \epsilon\vec{u}_B\cdot\nabla\vec{u}_B + \frac{\epsilon}{4}\vec{u}_T\cdot\nabla\vec{u}_T + \hat{f}\hat{k}\times\vec{u}_B = -\nabla\phi_B \tag{12}$$

$$\epsilon\frac{\partial}{\partial t}\vec{u}_T + \epsilon\vec{u}_T\cdot\nabla\vec{u}_B + \epsilon\vec{u}_B\cdot\nabla\vec{u}_T + \hat{f}\hat{k}\times\vec{u}_T = -\nabla\phi_T \tag{13}$$

$$\epsilon F_T\frac{\partial}{\partial t}\phi_T + \frac{1}{2}\nabla\cdot(\vec{u}_B + \frac{1}{2}\vec{u}_T) + \epsilon F_T\nabla\cdot[(\vec{u}_B + \frac{1}{2}\vec{u}_T)\,\phi_T] = 0 \tag{14}$$

$$\epsilon F_B\frac{\partial}{\partial t}\phi_B + \nabla\cdot\vec{u}_B + \frac{g'}{8g}\nabla\cdot\vec{u}_T + \epsilon F_T\nabla\cdot(\vec{u}_T\phi_T) + \epsilon F_B\nabla\cdot[(\vec{u}_B - \frac{1}{2}\vec{u}_T)\,\phi_B] = 0\,. \tag{15}$$

where the variables now are understood to be non-dimensional. We have assumed that $|g\chi| \approx |g'\eta|$ and that $|\phi_B| \approx |\phi_T| \approx f_0\,UL$. We also exploited the fact that $1 + g'/g \approx 1$. We will confine our attention to the β-plane, so that the non-dimensional Coriolis parameter is $\hat{f} = 1 + \beta Ly/f_0$, with f_0 the parameter value at the mid-basin. But we do not assume that the β term is small (as is usually done in deriving the QG expansion); the basin may be large.

The solutions will depend on three non-dimensional parameters. One is the Rossby number, $\epsilon = U(f_0 L)^{-1}$. In addition there are:

$$F_B \equiv \frac{f_0^2 L^2}{gH} \ , \quad F_T \equiv \frac{f_0^2 L^2}{g' H}$$

which are Burger numbers related to the external and internal deformation radii.

2.2 Basic wave

We consider first the large scale baroclinic wave, which we designate with capital variables (U, V, Φ_T, Φ_B). Since the relevant length scale is that of the basin, the Rossby number is small (for typical velocities). In addition, the barotropic Burger number, F_B, is order one and the baroclinic Burger number is large; we'll assume, for simplicity, that $F_T \approx \epsilon^{-1}$.

Because the wave is predominantly baroclinic, an appropriate expansion is:

$$\vec{u}_T = \epsilon \vec{U}_T + \epsilon^2 \vec{U}_T^{(2)} + ..., \quad \phi_T = \epsilon \Phi_T + \epsilon^2 \Phi_T^{(2)} + ... \tag{16}$$

$$\vec{u}_B = \epsilon^2 \vec{U}_B^{(2)} + ..., \quad \phi_B = \epsilon^2 \Phi_B^{(2)} + ... \tag{17}$$

The leading order wave term is order Rossby number because if it were order one, the wave would satisfy a Burger's equation and would thus steepen in time (e.g. Charney and Flierl, 1981). Note that we cannot assume the barotropic part of the field is zero because self-advection by the baroclinic wave excites barotropic motion at order ϵ^2. Substituting these expansions into the six non-dimensional equations yields, at order (Oϵ):

$$\hat{f}\hat{k} \times \vec{U}_T = -\nabla \Phi_T \tag{18}$$

$$\frac{\partial}{\partial t} \Phi_T + \frac{1}{4} \nabla \cdot \vec{U}_T = 0 \ . \tag{19}$$

which are familiar as the linearized planetary geostrophic equations. The wave velocities are geostrophic, but they are also divergent due to the variation in f. Combining equations (18) and (19) yields the long wave equation, which in dimensional form is:

$$\frac{\partial}{\partial t}\Phi_T - \frac{g'H\beta}{4f^2}\frac{\partial}{\partial x}\Phi_T = 0 \ , \tag{20}$$

The solution is a steadily-propagating wave with a phase speed which varies with latitude. The presence of boundaries requires the introduction of dissipation to satisfy the no-normal flow condition, but this is straightforward to do (e.g. LaCasce and Pedlosky, 2002).

2.3 Perturbations

Following LP04, we anticipate unstable growth near the deformation radius. If so, the perturbations will have a length scale which *varies with latitude*. The effective Rossby number will thus vary, although we assume nevertheless that it is small at all latitudes. In addition, the barotropic Burger number will be small (because the external deformation radius greatly exceeds the internal radius), but the baroclinic Burger number is order one and will vary in y. We assume in addition that $\beta L_D/f$ is small at all latitudes (and comparable to the Rossby number) and we neglect the term in (15) proportional to g'/g (i.e. we assume that ratio is smaller than the Rossby number).

Under these assumptions, the first-order momentum balances are:

$$\hat{k}\times\vec{u}_T = -\nabla\phi_T \ , \quad \hat{k}\times\vec{u}_B = -\nabla\phi_B \tag{21}$$

so that the velocities are geostrophic and non-divergent. In other words, the perturbations are *locally quasi-geostrophic*, which we term "LQG". The continuity equations at first order imply simply that the velocities are non-divergent, meaning the system is underdetermined. So one requires the order ϵ equations to solve the system, a familiar feature of the QG expansion (Pedlosky, 1987). Those equations can be combined into statements for the conservation of barotropic and baroclinic potential vorticity:

$$\frac{\partial}{\partial t}q_B + \vec{u}_B \cdot \nabla q_B + \frac{1}{4}\vec{u}_T \cdot \nabla q_T + \beta \frac{\partial}{\partial x}\phi_B = 0 \tag{22}$$

$$\frac{\partial}{\partial t}q_T + \vec{u}_B \cdot \nabla q_T + \vec{u}_T \cdot \nabla q_B + \beta \frac{\partial}{\partial x}\phi_T = 0 \tag{23}$$

where:

$$q_T \equiv \nabla^2 \phi_T - 4F_T(y)\,\phi_T, \quad q_B \equiv \nabla^2 \phi_B \ .$$

Now we must link up the perturbations and the baroclinic basic wave. To do this, we introduce into the expansion in section (2.2) perturbations with a second small parameter, α. So for example, one would write:

$$\phi_T = \epsilon \Phi_T + \epsilon^2 \Phi_T^{(2)} + \epsilon\alpha\phi_T + \ ...$$

The resulting expansion yields the LQG PV equations linearized about the baroclinic basic wave:

$$\frac{\partial}{\partial t}q_B + \frac{1}{4}\vec{U}_T \cdot \nabla q_T + \frac{1}{4}\vec{u}_T \cdot \nabla Q_T + \beta \frac{\partial}{\partial x}\phi_B = 0 \tag{24}$$

$$\frac{\partial}{\partial t}q_T + \vec{U}_T \cdot \nabla q_B + \vec{u}_B \cdot \nabla Q_T + \beta \frac{\partial}{\partial x}\phi_T = 0 \tag{25}$$

where:

$$Q_T \equiv \nabla \times \vec{U} - 4F_T(y)\,\Phi_T$$

is the basic wave potential vorticity.

Equations (24) and (24) are very similar to the QG stability equations examined by LP04. The major difference is that the baroclinic Burger number, F_T, varies with y, so that the system has non-constant coefficients. This hinders simple analytical solutions, but numerical solutions are feasible and we examine some hereafter.

3 LQG Results

3.1 Eigenmodes

We discretized the dimensional versions of equations (24) and (25) on the C-grid and solved them numerically. We did this in two ways. First we converted the equations to matrix form and solved the resulting eigenvalue problem. This is applicable to the high-Z limit of LP04, in which the wave is stationary to first order in $1/Z$. Then we examined the evolution of a propagating wave by stepping the equations forward in time. The eigenvalue calculation yields information on the structure and growth rates of the unstable disturbances, while the time-stepping reveals the combined action of the disturbances.

As a first example, we consider a wave which is sinusoidal in x and with a vertical shear which is invariant in y (except near the northern and southern boundaries where the wave is tapered). The invariance of the shear helps to highlight the latitudinal variation of the instability. In line with the high-Z limit, we neglect the β terms for both the basic wave and the instabilities. We calculated modes for a basin 1000 km wide (x direction) by 4000 km long (y direction), centered at 45 degrees north. The basin was 4000 m deep, with two equal layers; we took $g' = 0.02\, m\, sec^{-2}$. The wave shear was set at 10 cm/sec. We extracted the first 50 eigenmodes (in complex conjugate pairs) using the sparse eigenvalue routine in Matlab.

Three eigenmodes (modes 1, 20 and 45) are shown in figure (1). In the left panels are the basic wave with the barotropic eigenmodes superimposed; in the right are estimates of the meridional scale of the eigenmodes as a function of latitude, generated by the continuous wavelet transform.[1] The gravest mode is intensified in the north while the higher modes are shifted to the south. The wavelet spectra support this southward shift, and also indicate an increase to the south in the dominant meridional scales. The latter moreover vary in proportion with the local deformation radius.

Extracting the dominant y-scale for all fifty eigenvectors and plotting them against y

[1]The wavelet software, written by C. Torrence and G. Compo, is available at http://paos.colorado.edu/research/wavelets/.

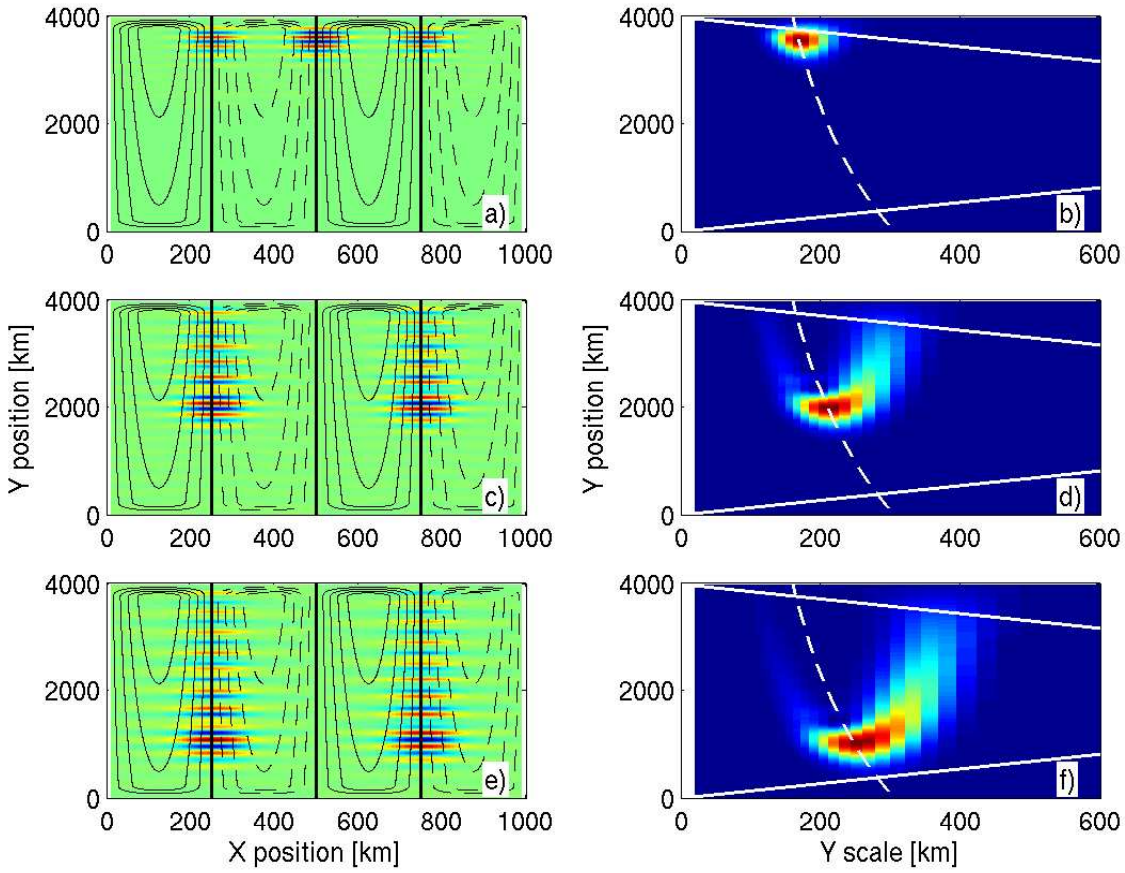

Figure 1: The barotropic perturbations for eigenmodes 1, 20 and 45 originating from a $\sin(kx)$ basic wave. The streamfunctions, with the eigenmodes superimposed, are shown at left. At right are wavelet transform power spectra, which indicate the dominant meridional scales as a function of latitude. The dashed line indicates a scale proportional to the local deformation radius. The upper and lower lines denote the "cones of influence" (COI) of the wavelet transform; the region of significance lies between the lines. The results outside the lines are adversely affected by the northern and southern boundaries.

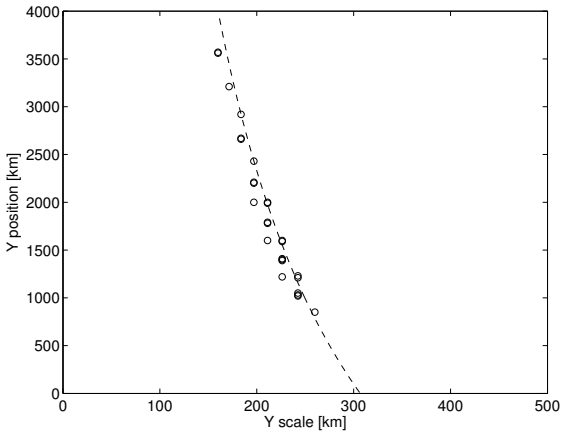

Figure 2: Estimates of the dominant meridional scale vs. y position derived from the wavelet spectra. The dashed line indicates one half the most unstable wavelength predicted from QG theory (from eq. 3.9a of LP04), which is proportional to the local deformation radius.

yields figure (2). As suggested, the scales vary in proportion to the local deformation radius. In fact, they are roughly equal to one half the most unstable wavelength predicted from QG theory (LP04) (which is also proportional to the deformation radius).

In figure (3) we plot the eigenmode growth rates vs. the y position of their maxima. The growth rates exhibit a linear dependence on the deformation radius, consistent with our earlier expectation (and also because the basic wave has a constant shear). The constant of proportionality, from a least squares fit, is within a factor of two of that predicted from QG theory.

Note that the higher modes also exhibit growth at higher latitudes at scales both larger and smaller than the deformation radius (Fig. 1). However this growth is slower than that in the deformation-scale growth in the lower modes. So the latter should dominate.

3.2 Time stepping

Next we time-step equations (24) and (25). This will permit examining what happens when the wave is actually propagating, as well as the cumulative effect of the unstable eigenmodes. We advance the equations using a fourth order Runge-Kutta scheme with an adaptive time step.

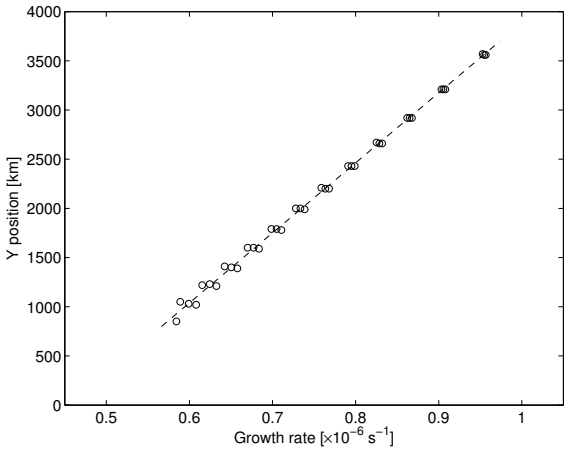

Figure 3: The modal growth rates at the latitudes corresponding to the wavelet spectra maxima. The dashed line comes from a least squares fit and indicates a linear dependence on the deformation radius.

Rather than using the sinusoidal wave of the previous section, we employ a wave which is localized initially near the eastern boundary. This is meant to approximate a wave excited by a Kelvin propagating along the eastern boundary (e.g. Milliff and McWilliams, 1994). The wave (shown in Fig. 4) is one wavelength of a sine wave, shifted by a constant so that the height is positive definite. The wave height is constant with latitude, except near the northern and southern boundaries where the wave is tapered. Moreover we take the wavelength to be 20 times the local deformation radius. This means that the vertical shear, with a value of 10 cm/sec, is constant with latitude.

The wave propagates as a long Rossby wave, under equation (20). The evolving wave is used for input to the stability equations (24-25) which are in turn advanced in time. We employ a domain which is 4000km-by-4000km (spanning roughly 40 degrees of latitude), centered at 30 degrees north. The basin depth and stratification were as in the eigenmode calculations. With a shear of 10 cm/sec, the Z values range from approximately 0.1 at the southern boundary to about 10 at the northern.

The evolution is depicted in figure (5), which shows the basic wave plus the unstable barotropic disturbances, and the wavelet specturm of the meridional scales of the latter. The basic wave propagates faster at low latitudes, causing the familiar latitudinal bending

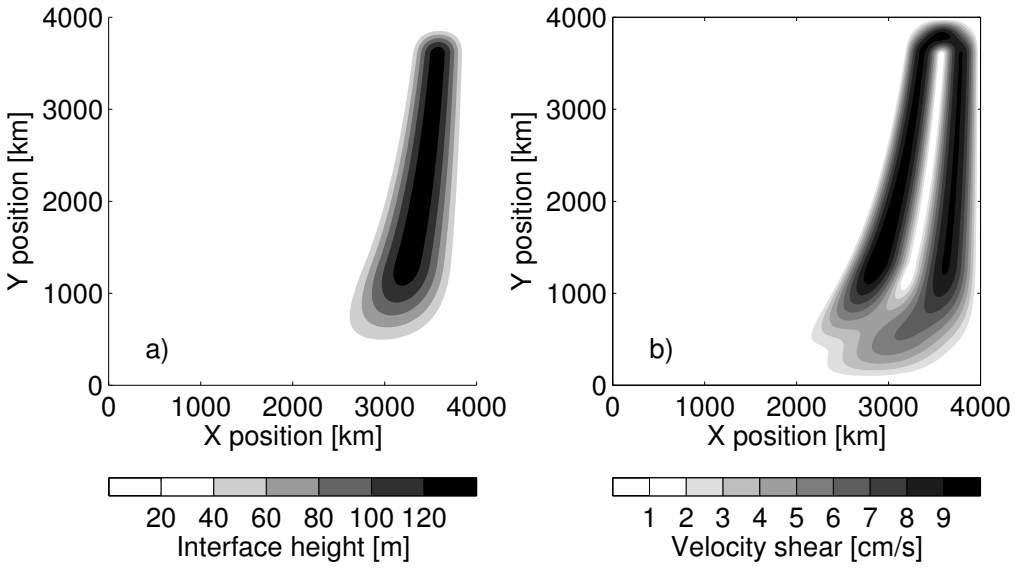

Figure 4: The eastern basin wave amplitude (left panel) and its vertical shear (right). The wavelength is 20 times the local deformation radius at all latitudes.

of the wave crests. The unstable disturbances appear first at high latitudes and intensify as the wave moves west; at low latitudes the growth is slower. The wavelet spectrum indicates the disturbances scale with the local deformation radius, and at a scale comparable to that predicted by QG theory. The spectrum also suggests larger scale features in the south, but these are for the most part insignificant.

The temporal growth of the barotropic perturbations is indicated in figure (6), which shows the rms barotropic pressure averaged in three latitude bands (centered at 860km, 1980 km and 3100 km). The results indicate clear exponential growth in the upper two latitude bands. The growth continues indefinitely in these simulations because the unchanging basic wave is effectively an infinite source of potential energy. Growth has commenced in the lowest band, but there is little increase before the basic wave strikes the western wall. Rescaling time by the expected growth time, L_D/U, we see that the growth rates in the northern two bands are similar. They are, moreover, comparable to the rate predicted by QG theory in the high-Z limit.[2]

[2]The QG low-Z growth rate for equal layer depths is $0.1U/L_D$ (LP04). This corresponds to a e-folding time of 10 times L_D/U. The high-Z growth rate is some 60 % faster.

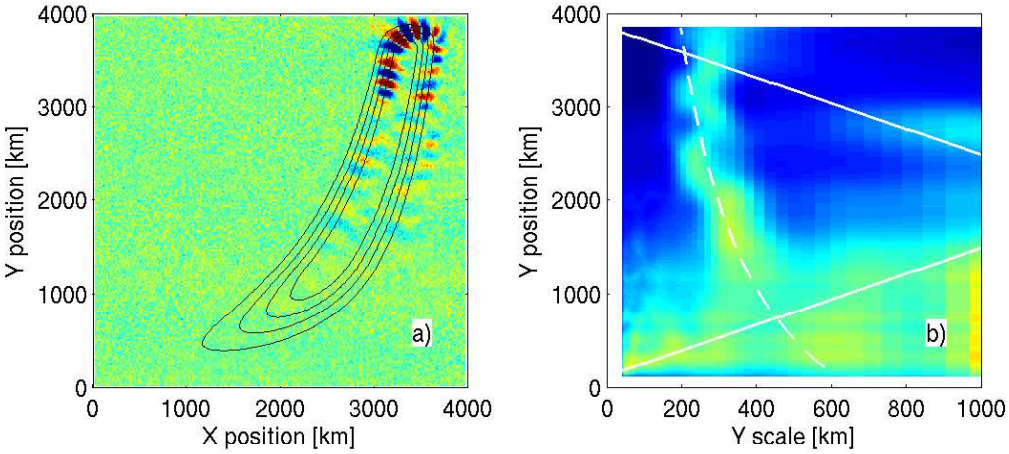

Figure 5: The LQG solution at day 75 for an isolated wave propagating from the eastern boundary. The wave is shown at left with the barotropic perturbations superimposed. At the right is the wavelet spectrum of the barotropic field, showing the dominant y-scale as a function of y (and normalized by the power at each y). The dashed line indicates one-half the wavelength of the most unstable wave predicted by QG theory and is proportional to the local deformation radius. The solid lines indicate the COI, defined in figure (1).

The LQG simulations thus support the idea of applying QG theory at successive latitudes. The large scale waves are unstable to deformation-scale perturbations whose growth times scale with the deformation radius. However the basic wave cannot change in these simulations, which means we can't see how the perturbations alter the basic wave. To see that, we must turn to a full ocean model.

4 Primitive equation simulations

The LQG expansion is based on the *assumption* of growth at the deformation radius and the LQG stability equations closely resemble those in QG. So it may seem unremarkable that the preceding results agree so well with QG theory. What we require is an independent means of examining the wave instability. For this we employ the Regional Oceanic Modelling System (ROMS; e.g. Shchepetkin and McWilliams, 2005). This model is based on the primitive equations and because of this, it is free of assumptions about the balances pertaining to the perturbations. Simulating large scale waves with the model will

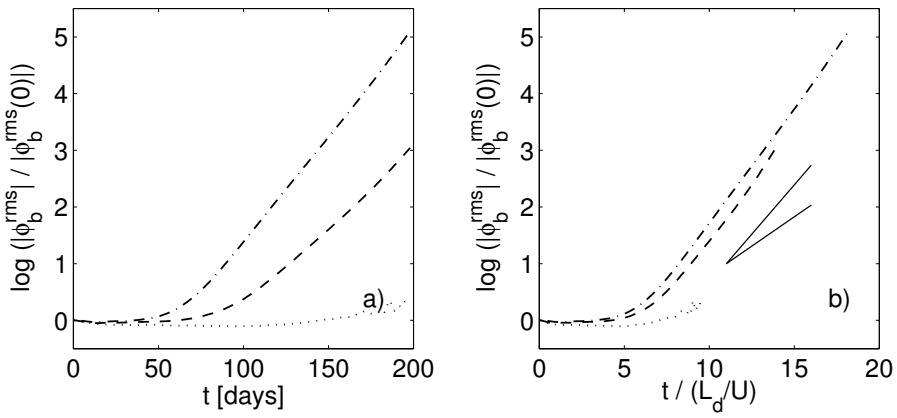

Figure 6: The rms barotropic pressure as a function of time for the isolated Rossby wave initiated near the eastern boundary. The curves correspond to latitude bands centered at 860 km (dotted), 1980 km (dashed) and 3100 km (dash-dotted). The two solid lines give theoretical growth curves in the low and high Z limits from the QG theory of LP04.

allow us to assess the LQG results and to test definitively whether the waves are unstable.

For the subsequent simulations, we used a spherical grid with a wedge-shaped sector spanning $160°$–$260°$ East, $5°$–$55°$ North. The model domain had 400 and 200 grid points in the zonal and meridional directions $(1/4° \times 1/4°)$, yielding a maximum horizontal grid spacing of 27 km (the deformation radius at the northern boundary, 25 km, is thus nearly resolved; it is resolved elsewhere). The bottom was flat, with a depth H=4000 m, and we used 10 vertical layers of equal thickness. All explicit mixing and dissipation was switched off, although there is small scale implicit dissipation associated with the model's third-order advection scheme (e.g. Ferziger and Pezic, 1999).

We initialized the model with a weak amplitude baroclinic wave (to approximate the order Rossby number baroclinic wave of section 2.2). We did not include the higher-order corrections, but rather let the model generate those itself (the correction fields are occasionally visible in the subsequent plots, in particular near the boundaries). We also added weaker, random barotropic and baroclinic perturbations, at 1/10 the amplitude of the basic wave, to catalyze the instability. In all cases, we retained a linear basic stratification (the baroclinic wave, being small in amplitude, represents a perturbation to this stratification). The buoyancy frequency was $0.0035\, rad\, sec^{-1}$; this is somewhat larger than typically ob-

served in the Pacific (Chelton et al., 1998), but yields larger deformation radii which are easier to resolve in these idealized runs.

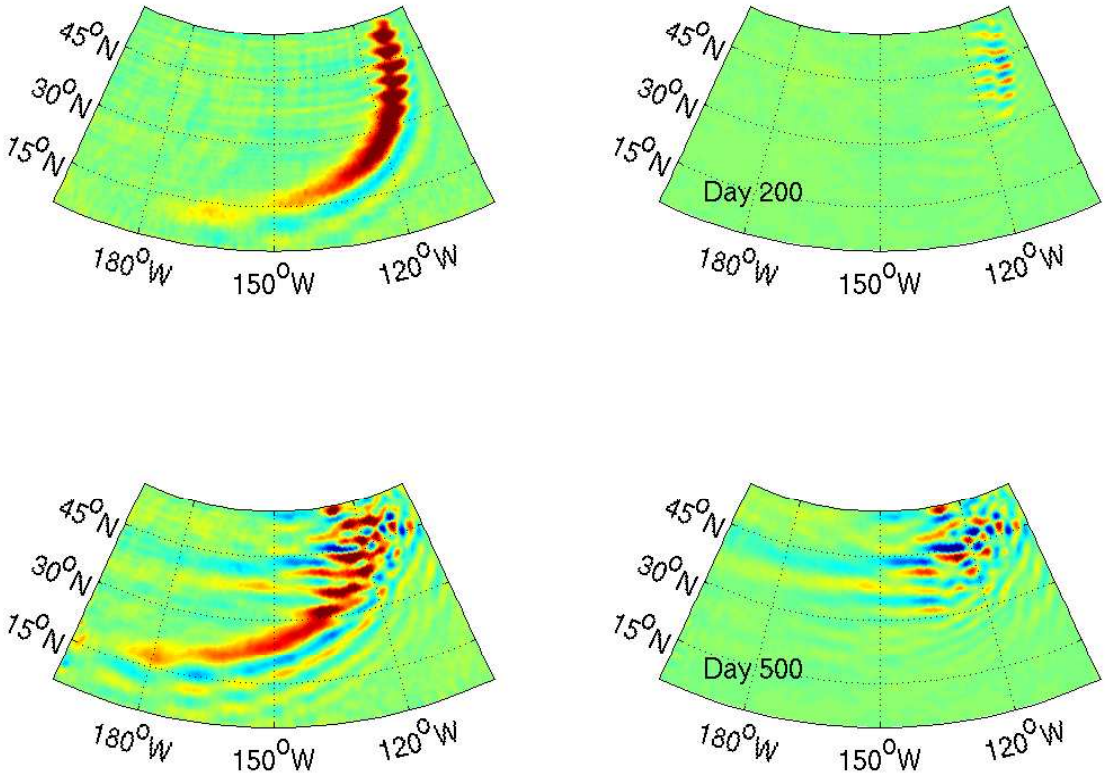

Figure 7: An initially isolated Rossby wave propagating from the eastern boundary. The wave structure is like that in figure (4), i.e. a single sine wave with a variable wavelength of 20 deformation radii. The sea surface elevation at days 200 and 500 are shown at left, and the barotropic height (defined in the text) at right. The color scale is from -10 cm to +10 cm.

We begin with the second case considered earlier, the isolated wave propagating from the eastern boundary. The initial condition was like that shown in figure (4), i.e. a single sine wave with a wavelength of 20 deformation radii. Shown in Figure 7 are the sea surface height and the barotropic displacement, at two different times. The displacement is calculated by integrating the geostrophic relation from the eastern boundary thus:

$$\eta_B = \frac{f}{g} \int_{xe}^{xe-x} v_B \, dx \tag{26}$$

where v_B is the depth-averaged meridional velocity.

As in the LQG simulation, the instabilities develop in the north first. By day 200, the perturbations north of 30 degrees are as strong as the wave and are severely distorting it. By day 500, the wave has broken up in the north and barotropic eddies are radiating to the west. Little unstable growth is seen south of 30 degrees, and the wave strikes the western boundary before breaking up.

Figure (8) shows the wavelet spectra of the meridional scales derived from the barotropic height field at three latitudes (17, 30 and 42 degrees). We use the barotropic height because it is more indicative of the perturbations than the actual surface height (which also reflects the basic wave). The spectra suggest growth in the upper two bands at a scale proportional to the deformation radius. The dominant wavelength is roughly $8L_D$, somewhat greater than $2\pi L_D$ and slightly greater than the scale seen in the LQG simulations.[3]

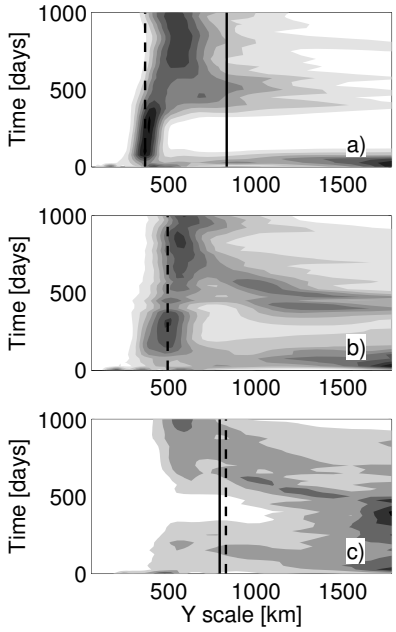

Figure 8: Wavelet spectra of meridional scale as a function of time, generated from the barotropic height at 17, 30 and 42 degrees of latitude. The dashed line indicates 1.3 times the deformation wavelength. The solid lines for the northern and southern latitudes are the COI of the transform (and reflect the effect of the nearby boundaries).

In the northern band, the energy shifts to larger scales at around day 500. This reflects

[3]Note the denominator of the dimensional Rossby dispersion relation is $k^2 + l^2 + L_D^{-2}$, so the wavelength corresponding to L_D^{-1} is $2\pi L_D \approx 6.3 L_D$. A factor of 8 is thus 1.3 times greater than this.

an inverse cascade of energy, as the barotropic eddies merge to produce larger eddies. The cascade however ceases, so that the scale remains fixed at the larger scale thereafter. The reason for the cessation is evidently the inhomogeneity in the eddy field, as discussed below. In the mid-latitude band there is also a shift to larger scales around day 500, but the shift is much less pronounced than in the north.

In the southern band, there is little indication of unstable growth. Rather there is energy at scales greater than 1500 km, which moreover is insignificant in the wavelet transform. There is significant energy below the deformation radius at late times, but this reflects the southward spreading of the unstable eddies from the north.

Figure (9) shows the growth rates at three latitudes, inferred from the rms barotropic height. The results suggest an increase in the barotropic energy in all three bands. There is transient, possibly exponential, growth followed by saturation. Plotting the rms height against time rescaled by L_D/U suggests the growth rates are roughly proportional to U/L_D and moreover are not greatly different from that predicted by QG theory.

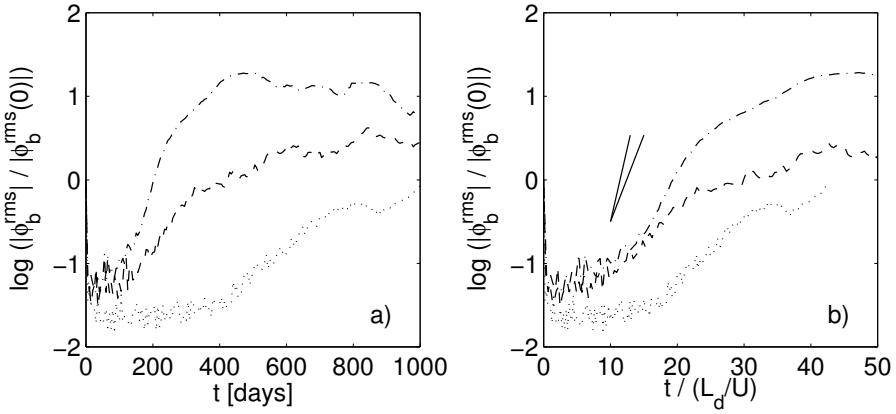

Figure 9: The rms barotropic height, averaged in three latitude bands centered at 17, 30 and 42 degrees, as functions of time. The rms heights are normalized by their initial values. The values are plotted against time on the left and against time rescaled by L_D/U on the right.

After about $20 - 30\, L_D/U$, the barotropic energy begins to level off. So growth saturation occurs after several e-folding times, as predicted by QG theory for the high-Z limit (see note in section 3.2). The ultimate energy level is greatest in the northern band,

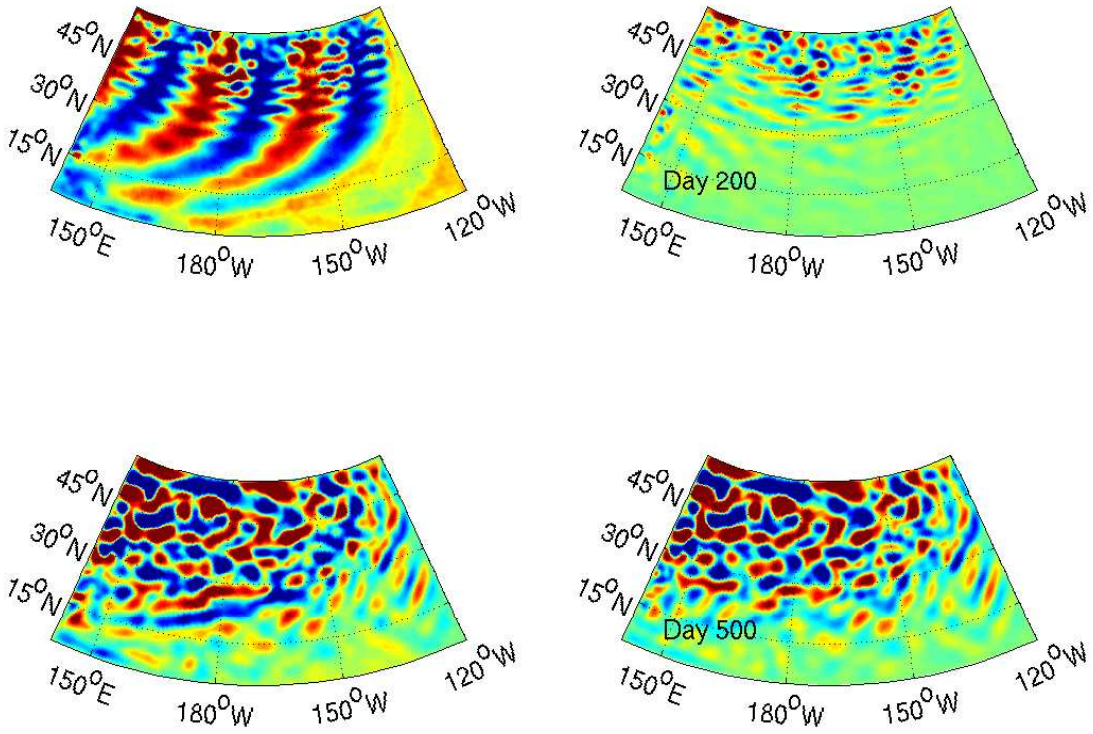

Figure 10: The sea surface and barotropic height fields for the initial sine wave, discussed in section (3.1) The color scale range is -20 to 20 cm.

implying a more energetic barotropic eddy field than elsewhere. This likely stems from having a constant wave shear, because there is more potential energy at high latitudes to be tapped by the instability.

The barotropic energy in the northern band saturates fully just after 400 days, which is roughly the same time as the barotropic energy shifts to larger scales (Fig. 8). So saturation there is coincident with the beginning of the energy cascade.

We also examined the sinusoidal wave considered in section (3.1). This wave differs from the eastern wave in that it spans the whole basin. Nevertheless the evolution of the height fields, shown in figure (10), is qualitatively the same. The wave breaks up in the north, on a time scale of several hundred days. The northern latitudes are then filled with barotropic eddies.

The change in scale of the barotropic eddies as function of time is seen in the wavelet

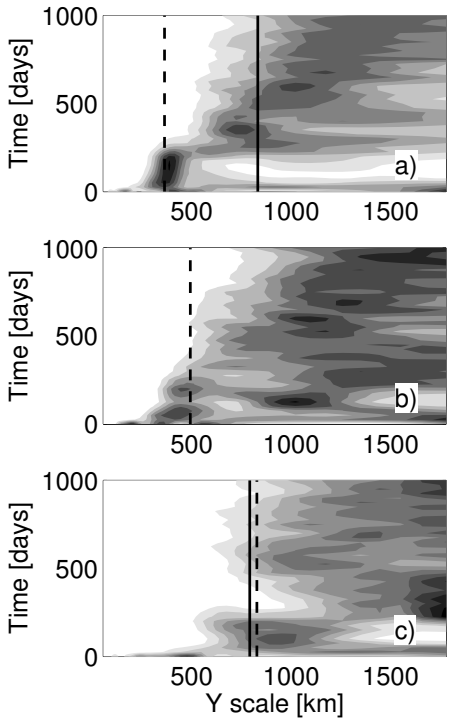

Figure 11: The wavelet spectra from the sine wave case. As before, the spectra were obtained from the rms barotropic height, averaged in three latitude bands. The dashed line indicates the same scale as in figure (8), or 8 times the deformation radius. The solid lines in the top and bottom panels are the COI.

spectra of meridional scales (Fig. 11). Looking at the northern and mid-latitude bands, we see energy appearing initially at the same scale as with the eastern wave (or 8 times deformation radius). Different from before though is that the energy begins to shift to larger scales earlier, around day 300, and that shift proceeds to still larger scales thereafter.

Evidently the inverse cascade is more energetic in this case, a consequence of having a more homogeneous barotropic eddy field. Unstable perturbations are growing in the east *and* west, and these eddies merge with one another. The isolated wave had a more localized eddy field, so the cascade could proceed essentially only to the scale of the initial wave. In other words, inhomogeneity in the eddy field in the eastern case causes the inverse cascade to cease, an effect noted by Rhines (1977). But with eddies everywhere, the cascade proceeds further upscale.

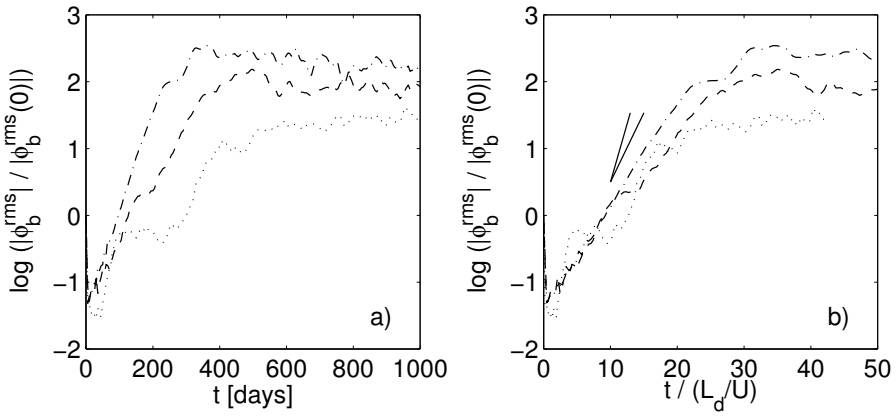

Figure 12: The rms barotropic height in the three latitude bands for the sine wave case, plotted against time and time rescaled by L_D/U.

The spectra from the southern band suggests energy at large scales. But due to the influence of the boundary, much of this is uncertain in the wavelet transform. As suggested in figure (10), the eddy field in the south is strongly affected by eddies spreading southward from the north.

The growth curves from the three latitude bands are shown in figure (12). As with the eastern wave, the curves indicate exponential growth, with rates comparable to that predicted by QG theory, followed by saturation. The latter occurs at a time of roughly 15-20 times L_D/U and roughly coincident with the shift in barotropic energy toward larger scales. The saturation energies are higher to the north, although the differences between latitudes are less than with the eastern wave.

So the ROMS simulations largely support the predictions of the LQG theory. The baroclinic Rossby wave is unstable to perturbations which grow at a scale proportional to the local deformation radius, L_D, with a growth rate proportional to U/L_D. The primary difference with the LQG simulations is that the perturbations grow to finite amplitude and merge, allowing for an inverse cascade of energy. This cascade is more energetic at high latitudes, owing to our choice of waves with constant shear. But the conclusion is the same, that at mid- to high latitudes the baroclinic wave gives way to barotropic waves.

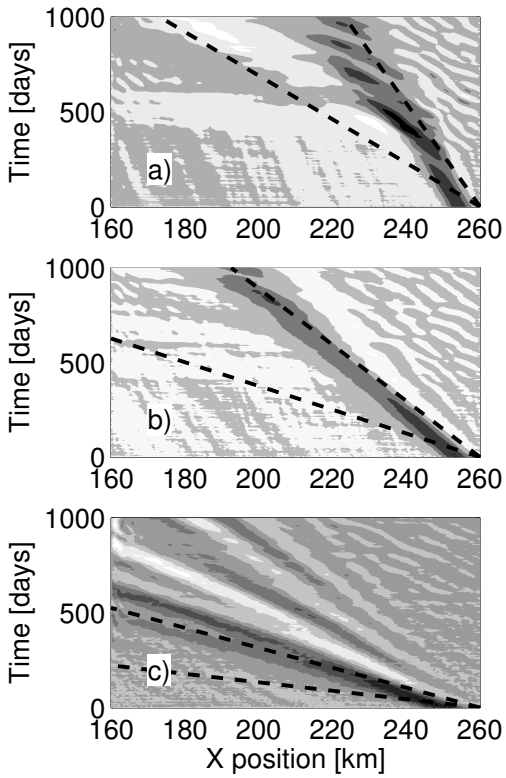

Figure 13: Hovmuller diagrams from the ROMS simulation of the isolated eastern wave. The diagrams were constructed from the sea surface height at the center latitudes from the three latitude bands examined earlier. The dashed lines indicate the long wave speed and 2.4 times that speed.

5 Phase speeds

The seminal observations of Chelton and Schlax (1996) suggested that the westward propagating sea surface height anomalies seen from satellite are moving faster than the baroclinic long wave speed outside the tropics. Subsequent theories attributed the increase in phase speed to a number of factors, including the interaction with the baroclinic mean circulation (Killworth et al., 1997) or topography (Tailleux and McWilliams, 2001).

LP04 suggested, rather, that wave instability at these latitudes might be responsible, if the height anomalies reflect *barotropic* rather than baroclinic Rossby waves. In particular, the most unstable barotropic wave from the QG theory has a phase speed roughly twice the long wave speed.

Here we examine the phase speeds in the ROMS simulations. We quantify these using

Hovmuller diagrams of the sea surface height. Figure (13) shows the diagrams from the isolated eastern wave case, using the height at the three latitudes considered earlier. The two dashed lines in the figure indicate the baroclinic long wave speed (the upper line) and the accelerated value (at 2.4 times the long wave speed; the lower line) predicted by LP04. Figure (14) shows the comparable Hovmuller diagrams from the sinusoidal wave case.

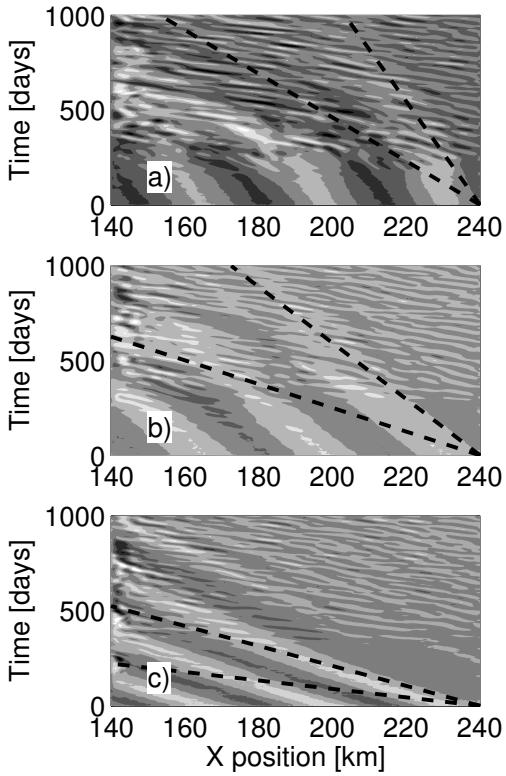

Figure 14: Hovmuller diagrams from the ROMS simulation of the sinusoidal wave. The dashed lines indicate the long wave speed and 2.4 times that speed.

In both figures, the crests in the southern band propagate at or near the long wave speed for the duration of the experiment.[4] At the mid- and high latitudes, the speeds increase mid-way through the experiment. At the northern-most latitude, the phase speed increase is evident after about 400 days in the eastern wave case and roughly 200 days in the sine wave case. The faster speeds in the eastern wave case are comparable to 2.4

[4]The additional crests seen in the eastern wave case are from shorter waves, propagating slower than the long wave speed, originating at the eastern boundary.

times the long wave speed. However they are even *faster* in the sine wave case.

Interestingly, the transitions to faster phase speeds occur roughly simultaneously with the shift to larger meridional scales (see figs. 8 and 11) and the saturation in unstable growth (figs. 9, 12). Evidently the phase speed increase is only visible after the baroclinic wave has broken up, so that the height field is dominated by the barotropic waves. During the growth phase, the baroclinic wave coexists with the perturbations, and the long wave speed is still evident. It is also possible that the barotropic perturbations are not propagating as fast as predicted by the QG theory. The latter prediction comes from the low-Z limit (pertaining to plane waves), in which the barotropic perturbations had zonal scales much longer than that of the basic wave. Here the barotropic perturbations grow in the high shear regions and propagate, at least initially, *with* the basic wave. So their phase speeds during the early growth period may indeed be similar to the long wave speed.

But regardless of the behavior during the adjustment, the apparent phase speeds are clearly faster than the long wave speed following the disintegration of the basic wave. The observed speeds in the eastern wave case are comparable to the 2.4 times the long wave speed, consistent with QG theory. The reason they are greater in the sine wave case is that the inverse cascade proceeds to larger scales, making larger—and thus faster—-barotropic waves.

We summarize the phase speed dependence on latitude in figure (15), which compares the speeds deduced from the height field with the long wave speed. We constructed this by extracting phase speeds from the Hovmuller diagrams at successive latitudes, for the two cases discussed. With the eastern wave, the speeds are comparable to the long wave speed south of 30 degrees, and 2-3 times higher north of that line. This is qualitatively consistent with the picture shown in Chelton and Schlax (1996; their figure 5). The sine wave case also exhibits faster waves, north of roughly 20 degrees, but the phase speeds are even faster, due to the active inverse cascade. As these speeds appear to be greatly in excess of those of Chelton and Schlax, we suspect such a cascade is probably *not*

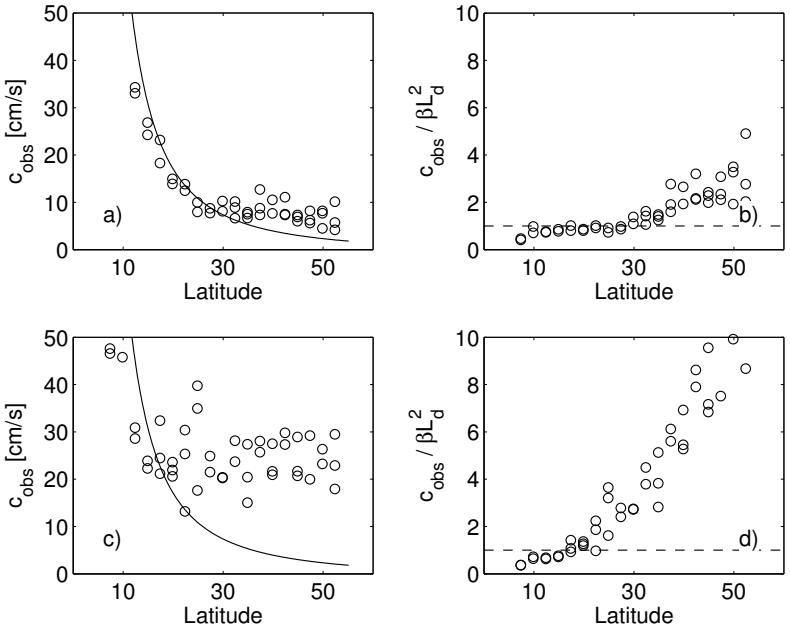

Figure 15: The westward phase speeds deduced from Hovmuller diagrams of the sea surface height in the ROMS experiments with the isolated eastern wave (upper panels) and the basin-spanning wave (lower panels). We extracted the speeds at the higher latitudes during the period just after the phase speed acceleration; at low latitudes, we extracted the speed from the leading wave crest. The right panels show the ratios of observed speed to the long wave speed. A more vigorous inverse cascade is responsible for the larger phase speeds in the lower panels.

occurring. This would imply that the eastern wave case is more realistic for the ocean than the basin-spanning sinusoidal wave.

6 Conclusions

We have generalized the quasi-geostrophic stability theory of LP04 to a realistically large ocean basin. To do this, we expanded the two layer shallow water equations by assuming a small-amplitude basin-scale wave and derived a pair of coupled stability equations. We refer to these as the "LQG" equations because they imply that the disturbances, anticipated to be of deformation-scale, are locally quasi-geostrophic. The LQG equations are similar to the barotropic/baroclinic QG vorticity equations, except that they retain a realistic variation of the deformation radius.

We examined instabilities arising from these equations by calculating eigenmodes of

the equations (assuming the wave was stationary) and then by time-stepping them. The eigenmode calculation suggested the most rapid growth at any latitude occurs near the deformation radius and that the growth rate is inversely proportional to the deformation radius. So instability proceeds most rapidly at high latitudes. The time-stepping yielded similar results and implied that only at southern latitudes could the wave cross the basin before succumbing to instability.

The results are thus in line with what would be expected by applying QG theory at successive latitudes. However, the LQG equations are very similar to their QG counterparts, so we then used a primitive equation model (the ROMS model) to obtain an independent confirmation. The ROMS results were indeed in line with the LQG results, showing unstable growth near the deformation radius with a time scale proportional to L_D/U.

Lastly we examined the westward phase speeds, apparent in the surface height field. As suggested by LP04, there is an increase in the speed following instability, because the barotropic waves (which have a surface expression) propagate faster than the baroclinic long wave speed. The increases seen with a case of an isolated wave emanating from the eastern wall were in excellent agreement with the satellite observations of Chelton and Schlax (1996).

Though we did not discuss it here, we also examined the instability of baroclinic basin modes. Indeed, the present work (and that of LP04) were motivated by the question of whether basin modes are unstable. The modes, discussed by LaCasce (2000), Cessi and Primeau (2001), Primeau (2002), LaCasce and Pedlosky (2002) and Ben Jelloul and Huck (2003), have very large scales and low frequencies, and are thus of potential interest for climate variability. We performed simulations of several different modes using both the LQG and ROMS models and all indicated that the modes were unstable. The instabilities grow fastest in the northwest, where the shear is greatest. But the conclusion is the same, that the modes, like the Rossby waves, break up at the northern latitudes.

Our focus has been on waves with fixed vertical shear, but oceanic waves emanating from eastern boundaries will have different amplitudes, depending on the forcing. This will impact the degree of penetration into the basin, by altering the unstable growth times. We have also neglected mean flow effects. However, if the primary dynamic is that of waves radiating from the eastern boundary, such waves may not have a chance to encounter significant mean flow, intensified in the west, before succumbing to instability. This remains to be seen of course with more realistic models. Furthermore, we have concentrated on weak amplitude waves, because finite amplitude Rossby waves would steepen in time (sec. 2.2). However, such waves would have stronger vertical shear and thus might be even more prone to instability. The analgous stability equations for an order one baroclinic wave are similar to those considered here, but with additional terms due to barotropic interactions; they could be studied in future.

There is also the fate of the barotropic eddies. Comparing our results with the satellite observations of Chelton and Schlax, it appears there is little in the way of an inverse cascade after instability. Stammer's (1997) results also argue against a cascade, because a cascade should be arrested by the β-effect (Rhines, 1977) and there is little evidence of a such arrest from the eddies seen in the height field. The cascade may be halted by the inhomogeneity of the eddy field or by another effect, like topography. But either way, the product of the instability would appear to be deformation-scale barotropic Rossby waves.

Finally, Rossby wave instability could have profound implications for the adjustment of wind-driven oceanic flows. Our general conception of the response to changing winds, following Anderson and Gill (1975), is of one mediated by Rossby waves propagating from the eastern boundary. The passage of the baroclinic waves alters the baroclinic structure of the general circulation. Instability of the baroclinic waves will presumably alter this process significantly. We are currently exploring this issue.

Acknowledgments

PEI was supported by a post-doctoral grant from the Norwegian Research Council, JHL supported under the Norwegian NOCLIM II program and JP was partly supported by NSF OCE 0451086.

References

Anderson, D.L.T. and A.E. Gill, 1975. Spin-up of a stratified ocean with application to upwelling. Deep-Sea Res., **22**, 583-596.

Ben Jelloul, M. and T. Huck, 2003. Basin-mode interactions and selection by the mean flow in a reduced-gravity quasigeostrophic model. J. Phys. Oceanogr., **33**, 2320-2332.

Cessi, P. and F. Primeau, 2001. Dissipative selection of low-frequency modes in a reduced-gravity basin. J. Phys. Oceanogr., **31**, 127-137.

Charney, J.G. and G.R. Flierl, 1981. Oceanic analogues of large-scale atmospheric motions. In *The Evolution of Physical Oceanography*, C. Wunsch and B. Warren, eds. MIT Press, 504-548.

Chelton, D. B. and M. G. Schlax, 1996. Global observations of oceanic Rossby waves. *Science*, **272**, 234-238.

Chelton, D. B., R. A. deSzoeke, M. G. Schlax, K. El Naggar and N. Siwertz, 1998. Geographical variability of the first-baroclinic Rossby radius of deformation. J. Phys. Oceanogr., **28**, 433-460.

Ferziger, J.H. and M. Peric, 1999. *Computational methods for fluid dynamics*. Springer-Verlag, 400 pp.

Killworth, P.D., D. B. Chelton and R. A. de Szoeke, 1997. The speed of observed and theoretical long extratropical planetary waves. J. Phys. Oceanogr., **27**, 1946-1966.

LaCasce, J.H., 2000. Baroclinic Rossby waves in a square basin. J. Phys. Oceanogr., **30**, 3161-3178.

LaCasce, J.H. and J. Pedlosky, 2002. Baroclinic Rossby waves in irregular basins. J. Phys. Oceanogr., **32**, 2828-2847.

LaCasce, J. H. and J. Pedlosky, 2004. The instability of Rossby basin modes and the oceanic eddy field. J. Phys. Oceanogr. **34**, 2027-2041.

Milliff, R. F. and J. C. McWilliams, 1994. The evolution of boundary pressure in ocean basins. J. Phys. Oceanogr., **24**, 1317-1338.

Pedlosky, J., 1987. *Geophysical Fluid Dynamics*. Springer, 728 pp.

Primeau, F. 2002. Long Rossby wave basin-crossing time and the resonance of low-frequency basin modes. J. Phys. Oceanogr., **32**, 2652-2665.

Rhines, P., 1977. The dynamics of unsteady currents. In *The Sea*, vol. 6, Wiley Interscience, NY, 189-318.

Stammer, D., 1997. Global characteristics of ocean variability estimated from regional TOPEX/POSEIDON altimeter measurements. J. Phys. Oceanogr., **27**, 1743-1769.

Tailleux, R. and J.C. McWilliams, 2001. The effect of bottom pressure decoupling on the speed of extratropical, baroclinic Rossby waves. J. Phys. Oceanogr., **31**, 1461-1476.